

# Digital twinning of self-sensing structures using the statistical finite element method

Eky Febrianto<sup>1,3</sup>, Liam Butler<sup>2,3</sup>, Mark Girolami<sup>1,3</sup> and Fehmi Cirak<sup>1,3\*</sup>

<sup>1</sup>Department of Engineering, University of Cambridge, Trumpington Street, Cambridge, CB2 1PZ, UK

<sup>2</sup>Lassonde School of Engineering, York University, Toronto, ON M3J 1P3, Canada

<sup>3</sup>The Alan Turing Institute, 96 Euston Road, London, NW1 2DB, UK

\*Corresponding author. E-mail: [f.cirak@eng.cam.ac.uk](mailto:f.cirak@eng.cam.ac.uk)

**Keywords:** digital twin, Bayesian learning, physics-informed machine learning, structural health monitoring, statistical finite element method, FBG sensing

## Abstract

The monitoring of infrastructure assets using sensor networks is becoming increasingly prevalent. A digital twin in the form of a finite element model, as used in design and construction, can help make sense of the copious amount of collected sensor data. This paper demonstrates the application of the statistical finite element method (statFEM), which provides a consistent and principled means for synthesising data and physics-based models, in developing a digital twin of a self-sensing structure. As a case study, an instrumented steel railway bridge of 27.34 m length located along the West Coast Mainline near Staffordshire in the UK is considered. Using strain data captured from fibre Bragg grating (FBG) sensors at 108 locations along the bridge superstructure, statFEM can predict the ‘true’ system response while taking into account the uncertainties in sensor readings, applied loading and finite element model misspecification errors. Longitudinal strain distributions along the two main I-beams are both measured and modelled during the passage of a passenger train. The digital twin, because of its physics-based component, is able to generate reasonable strain distribution predictions at locations where no measurement data is available, including at several points along the main I-beams and on structural elements on which sensors are not even installed. The implications for long-term structural health monitoring and assessment include optimisation of sensor placement, and performing more reliable what-if analyses at locations and under loading scenarios for which no measurement data is available.

## 1. Introduction

Designers, engineers and maintenance managers often rely upon computer simulations such as finite element (FE) models to help better understand the current and future behaviour of infrastructure assets. These models have traditionally been used to either facilitate the design of a newly constructed structure or to help with the assessment of a structure which has been in operation for many years. The level of sophistication of these models often depends upon the purpose for which they are being constructed, the structure that is being modelled, and the resources available (i.e., technical skill, time, computational power, etc.). As with any mathematical model, FE models involve assumptions and parameters, which are inevitably subject to uncertainties, both epistemic and aleatoric, and require engineers with a sufficient degree of experience to properly verify and interpret the predicted results (Oden et al., 2010; Lau et al., 2018).

Conversely, a trend towards monitoring of infrastructure assets using sensors, see the reviews (Abdulkarem et al., 2020; Lynch, 2007; Brownjohn, 2007), has led to the development of new

and powerful data-driven approaches to model infrastructure performance. Specifically, sensing can generate performance information to help inform when to inspect, repair or decommission a structure; help to provide evidence for extending the life of a structure; and accelerate and improve prototyping of new materials (Frangopol and Soliman, 2016). There have been a wide array of field studies which have implemented sensing in bridges, tunnel linings, high-rise buildings, and dams. For instance, De Battista et al. (2017) instrumented several columns and walls at every floor in a 50-storey residential building in central London. Using distributed fibre optic sensors (DFOS), they were able to measure the axial shortening of the various columns and walls as the building was being erected. The data from these sensors were used to validate engineering models and to assist the contractor with construction. Recently, Di et al. (2021) reported a study whereby electrical-based strain gauges were installed on a 450 metre steel tied-arch bridge with an orthotropic steel deck. These types of bridge structures are particularly susceptible to fatigue damage and, using the data captured via the sensors, they were able to identify several fatigue-vulnerable locations along the structure. The structural health monitoring system was further used to validate a FE model of the bridge which incorporated a novel, ultra-high performance concrete bridge deck which was proposed as a measure to reduce the risk of fatigue cracking. Another unique application of structural health monitoring of a 100 metre segment of tunnel lining at the CERN (European Council for Nuclear Research) was conducted by Di Murro et al. (2016). Localized tension and compression cracks were observed in the tunnel and prompted instrumentation and monitoring using DFOS. Based on data captured over 10 months, they reported strain levels in the tunnel which ultimately proved to be insignificant.

With the increase in structural health monitoring campaigns being undertaken around the globe, the infrastructure engineering sector has been inundated with large quantities of data whose value is still being realized. In particular, this emerging sensing paradigm has resulted in the development of new data-driven approaches to model infrastructure performance; see the extensive discussions Huang et al. (2019); Wu and Jahanshahi (2020). Unlike, FE modelling, data-driven (statistical) approaches utilising monitoring data provide information about the actual operational performance of a particular piece of infrastructure. The modelling effort associated with data-driven techniques is comparatively lower than in FE modeling. However, even the most sophisticated data-driven models, which employ artificial neural networks, Gaussian process regression or Bayesian model updating require a copious amount of *real-world* training data upon which to make predictions. This contrast between FE-based and data-driven approaches is further elaborated in Ye et al. (2019) who discuss a hybrid or digital twin-based approach. These challenges have prompted research in the areas of model updating and system identification which have attempted to use both FE models and data-driven models (i.e., derived from sensor data) to provide better predictions of system behaviour, see e.g. Malekzadeh et al. (2015); Pasquier and Smith (2016); Tsialiamanis et al. (2021). The current modelling approaches, however, seem to be not able to synthesize measurement data with uncertainties and predictions from inherently misspecified FE models, in a manner which allows for the generation of continuous predictions as new measurement data becomes available. This ability is critical for the realisation of digital twins (Rasheed et al., 2020; Worden et al., 2020). In its broadest sense, as defined in a UK governmental report, a digital twin is a realistic digital representation of assets, processes or systems in the built or natural environment (Bolton et al., 2018).

Recently, Girolami et al. (2021) proposed a statistical construction of the FE method, dubbed as stat-FEM, which allows one to make predictions about the true system behaviour in light of measurement data. Adopting a Bayesian viewpoint, any lack of knowledge, or uncertainty, associated with the errors in the collected data, choice of the FE model and its parameters are treated as random variables. For a discussion on the Bayesian viewpoint in structural health monitoring see, e.g., Beck (2010) or Huang et al. (2019). As an example, in the case of the railway bridge considered in this study, the as-built dimensions, support conditions and train loadings are all only partially known and can be considered as random variables. Starting from some chosen prior probability densities for the random variables, consolidating any knowledge at hand, Bayes rule provides a coherent formalism to infer, or learn, their respective posterior densities while making use of the likelihood of the observations. In general, the

posterior probability densities become more concentrated than the prior densities and can be expected to converge towards the true non-random values with increasing amount of data in a well-formulated problem (Stuart, 2010; Kaipio and Somersalo, 2006). Following Kennedy and O’Hagan (2001), in statFEM the observed data  $\mathbf{y}$  is equated to three random components, namely a FE component  $\mathbf{u}$ , a model misspecification component  $\mathbf{d}$  and a measurement noise component  $\mathbf{e}$ . Each of the random components may depend on additional random *hyperparameters* with respective prior probability densities. In this study, only the model misspecification component  $\mathbf{d}$  has hyperparameters. The posterior densities of the FE component  $\mathbf{u}$ , the true system response  $\mathbf{z} = \mathbf{u} + \mathbf{d}$  and the hyperparameters are determined by applying Bayes rule on two different levels in turn. The prior probability density of the FE component  $\mathbf{u}$  is obtained by solving a traditional probabilistic forward problem with a random applied forcing. The overall approach is akin to the empirical Bayes or evidence approximation techniques prevalent in machine learning (MacKay, 1992, 1999; Murphy, 2012). Finally, a key difference between statFEM and the seminal Kennedy and O’Hagan Kennedy and O’Hagan (2001) approach on calibration and related follow-on papers (Bayarri et al., 2007; Arendt et al., 2012; Santner et al., 2018) concerns the FE component  $\mathbf{u}$ . In statFEM,  $\mathbf{u}$  is obtained by solving a classical probabilistic forward problem (Sudret and Der Kiureghian, 2000; Ghanem and Spanos, 1991) instead of obtaining it from a given computer code (simulator) by regression.

This paper evaluates the application of statFEM to the development of a statistical digital twin of the superstructure of an operational railway bridge, see Figure 1. The newly constructed skewed half-through bridge has previously been instrumented with a network of fibre optic based sensors. The instrumentation of the bridge using FBG strain sensors is described in Butler et al. (2018). The sensor measurements have since been compared with a deterministic FE model of the bridge in Lin et al. (2019). The contributions from this work are threefold including: (1) the introduction of a new modelling paradigm for use in structural health monitoring; (2) evaluating the trade-off between number of sensing measurements and FE model complexity; and (3) introducing the concept of a statistical digital twin by demonstrating the application of statFEM to real-time strain sensing.

The outline of this paper is as follows. In Section 2, the structural system of the railway bridge and its instrumentation with FBG sensors are introduced. The proposed statistical digital twin of the

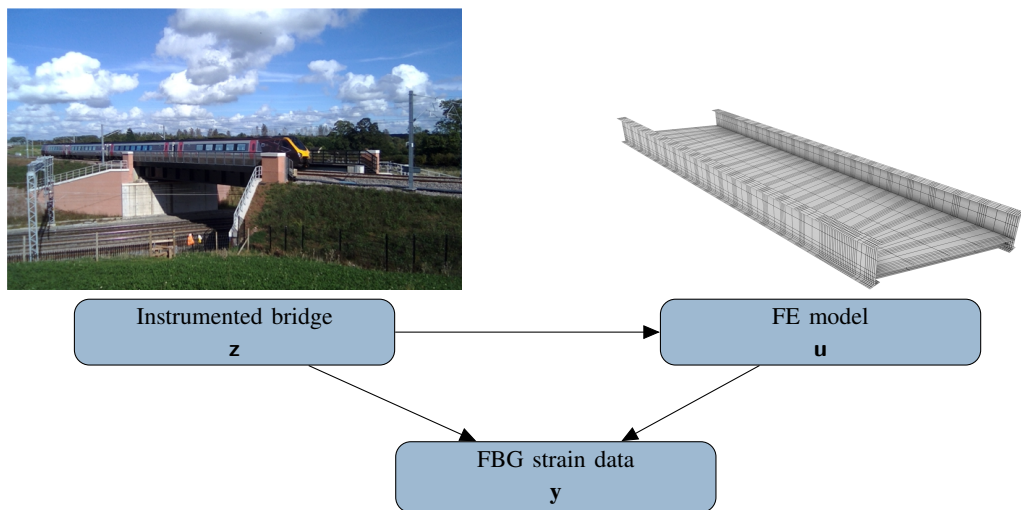


**Figure 1.** Railway intersection bridge (west elevation), a representative finite element discretisation and the statistical model underlying statFEM. The response of the bridge  $\mathbf{z}$ , the strain data vector  $\mathbf{y}$  observed using FBG sensors and the finite element response  $\mathbf{u}$  are all random. The random vectors depend in turn on additional random hyperparameters.

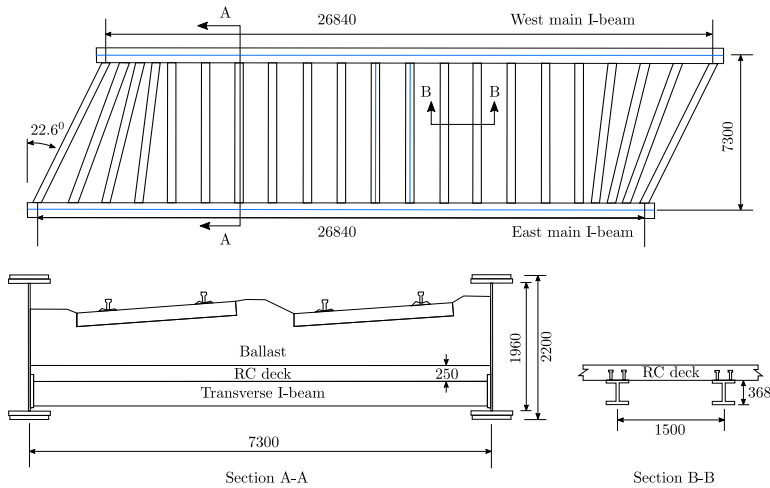


**Figure 2.** Dimensions of the bridge superstructure (all in mm).

superstructure is discussed in Section 3. To this end, first the statistical finite element method is reviewed in Section 3.1, and then the FE model of the structure is presented in Section 3.2. In Section 4, the obtained digital twin is used to infer the true strain distribution over the entire structure during the passage of a train. In particular, it is shown that the inference results are largely insensitive to the number of sensors and sampling frequency confirming the utility of a statFEM model as an integral part of a digital twin. Lastly, Section 5 concludes the paper and discusses several promising directions for future research.

## 2. Self-sensing railway bridge

### 2.1. Structural system

Completed in 2016, Intersection Bridge 20A is a 27.34 m steel skewed half-through railway bridge located along the West Coast Mainline near Staffordshire in UK (Figure 1). The bridge carries two lines of passenger trains (with speeds up to 160 km/h) over another heavily trafficked rail corridor along the West Coast Main Line. The superstructure consists of a pair of steel main I-beams and 21 transverse I-beams spanning the 7.3 m width of the structure, see Figure 2. The two main I-beams (referred to as east and west) are 26.84 m long and 2.2 m deep (including doubler plates). Web stiffeners installed along the outside web of the main I-beams are used to improve stability and to prevent local buckling of the main I-beams' web and top flanges. Four rocker-type bearings, which sit atop reinforced concrete abutments support the main bridge superstructure.

The transverse I-beams are 368 mm deep and the attached shear stud connectors provide for the composite action with the reinforced concrete deck slab. The transverse beams are spaced at every 1.5 m in the middle of the bridge, and are fanned closer towards the two ends of the bridge. Pinned and moment connections are used to link the transverse and the main I-beams. A 250 mm thick reinforced concrete deck slab spans between transverse beams and supports the ballasted track bed system. The ballast has the minimum depth of 300 mm and supports concrete sleepers to which the rails are fastened.

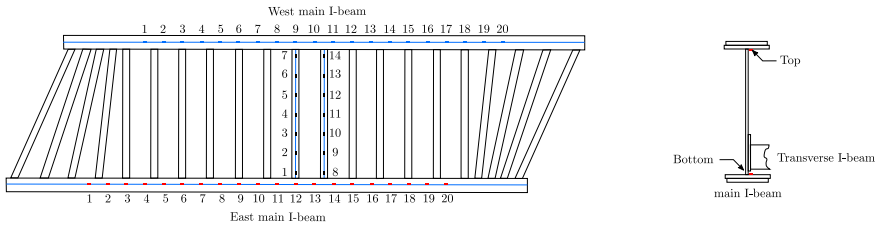


**Figure 3.** Position and numbering of the FBG strain sensors installed on the bridge. The same numbering is used for the sensors at both top and bottom flanges. Not to scale.

## 2.2. Sensor instrumentation

This recently constructed bridge was instrumented with an innovative fibre optic based sensor (FOS) network which was designed to provide reliable and long-term measurements of the bridge's operational performance (Butler et al., 2018). As depicted in Figure 3, FBG sensors were installed on the main structural elements. The sensor arrays used as part of this study had up to 108 strain FBGs. Along the east main I-beam, 20 FBGs were placed at one metre spacing along both the top and bottom flanges. Similarly, the same sensor arrangement is installed along the west main I-beam (i.e., 40 FBGs per I-beam). The other 28 FBGs are located along the top and bottom flanges of two adjacent transverse I-beams close to the midspan of the main I-beams. The position and numbering of the 108 FBG sensors installed on the structure is as shown in Figure 3.

The sensors installed were based on FBG technology which can measure strain and temperature at discrete points along an optical fibre. Consisting of glass fibres, FOS are lightweight, require minimal number of wiring cables and provide stable long-term measurements. When laser light is shone down a fibre optic cable, the gratings act like dielectric mirrors reflecting only those wavelengths, which match the Bragg wavelength. When the fibre optic cable is elongated (or shortened), the wavelength of the reflected light shifts in proportion to this change in strain. Once a fibre optic cable is attached to a structure, the cable can be used to measure changes in strain of the structure itself. The mechanical strain can be calculated by removing temperature effects associated with the thermal expansion of glass, the effect of temperature on the index of refraction of glass, and the thermal expansion of the substrate material (i.e. steel) using (Butler et al., 2018)

$$\Delta\epsilon_m = \frac{1}{k_\epsilon} \left( \left( \frac{\Delta\lambda}{\lambda_0} \right)_S - k_T \frac{\left( \frac{\Delta\lambda}{\lambda_0} \right)_T}{k_{T_T}} \right) - \alpha_{\text{sub}} \frac{\left( \frac{\Delta\lambda}{\lambda_0} \right)_T}{k_{T_T}}, \quad (1)$$

where  $\Delta\epsilon_m$  is the change in mechanical strain;  $(\Delta\lambda/\lambda_0)_S$  is the change in relative wavelength of the strain sensor;  $(\Delta\lambda/\lambda_0)_T$  is the change in relative wavelength of the temperature-compensating sensor;  $k_\epsilon$  is the gauge factor provided by the strain FBG manufacturer (typically 0.78);  $k_T$  is the change of the refractive index of glass;  $k_{T_T}$  is the experimentally derived constant for the FBG temperature-compensating sensor; and  $\alpha_{\text{sub}}$  is the linear coefficient of thermal expansion of the substrate material (concrete:  $10 \times 10^{-6} / ^\circ\text{C}$ ; steel:  $12 \times 10^{-6} / ^\circ\text{C}$ ). Each FBG is capable of recording strain with an accuracy of approximately  $\pm 5 \cdot 10^{-6}$  at a data acquisition rate of up to 250 Hz.

Monitoring data were captured by the sensor network beginning from the time that the bridge was being constructed (Butler et al., 2018). Following the construction, the bridge was monitored sporadically for two years (Lin et al., 2019). During this period, FBG data were captured for the passage of more than 130 individual trains. This dataset contains strain data for the passage of two passenger train types: the London Midland Class 350 Desiro (type T1) and the Cross Country Class 221 Super Voyager (type T2). Both train types included 4 or 5-car configurations. Their axle weightings and spacing were provided by Network Rail, the UK's national rail authority.

### 3. Statistical Digital Twin

#### 3.1. Review of the statistical finite element method

This section introduces the computational model of the bridge superstructure and provides a brief review of the statFEM for synthesising observation data into the computational model, i.e. the digital twin. The main source of uncertainty for the obtained digital twin is assumed to be due to the train loading, which is only partially known. In the FE model inertia effects are neglected, due to the relatively short span of the bridge, so that a static rather than a dynamic analysis is sufficient (Lin et al., 2019).

##### 3.1.1. Probabilistic forward FE model

The bridge superstructure is modeled using isogeometrically discretised Kirchhoff-Love shell finite elements (Cirak et al., 2000, 2002; Cirak and Long, 2011). The shell model takes into account the in-plane membrane and out-of-plane bending response of the structural members. The FE model of the superstructure, consisting of the main girders, cross beams and the reinforced concrete deck, is obtained by rigidly connecting horizontally and vertically aligned plates, i.e. initially planar shells, along joints. Consequently, the joints are able to transfer both forces and moments.

The weak form of the shell equilibrium equation, or the principle of virtual work, for a Kirchhoff-Love shell with the midsurface  $\Omega$  and the position vector  $\mathbf{x}$  reads

$$\int_{\Omega} (\mathbf{n}(\mathbf{x}) : \delta\boldsymbol{\alpha}(\mathbf{x}) + \mathbf{m}(\mathbf{x}) : \delta\boldsymbol{\beta}(\mathbf{x})) \, d\Omega = \sum_j \mathbf{f}^{(j)} \cdot \delta\mathbf{u}^{(j)} + \int_{\Omega} \mathbf{r}(\mathbf{x}) \cdot \delta\mathbf{u}(\mathbf{x}) \, d\Omega. \quad (2)$$

Here, the penalty term enforcing the conformity of the displacements and rotations of all plates attached to the same joint has been omitted for the sake of brevity. The internal virtual work on the left-hand side depends on the membrane force resultant  $\mathbf{n}(\mathbf{x})$ , the bending moment resultant  $\mathbf{m}(\mathbf{x})$ , the virtual membrane strain  $\delta\boldsymbol{\alpha}(\mathbf{x})$  and the virtual bending strain  $\delta\boldsymbol{\beta}(\mathbf{x})$ . Evidently, these fields depend in turn either on the displacements  $\mathbf{u}(\mathbf{x})$  or the virtual displacements  $\delta\mathbf{u}(\mathbf{x})$ . Furthermore, we assume a linear elastic and isotropic material so that the two resultants  $\mathbf{n}(\mathbf{x})$  and  $\mathbf{m}(\mathbf{x})$  depend on the respective strains  $\boldsymbol{\alpha}(\mathbf{x})$  and  $\boldsymbol{\beta}(\mathbf{x})$  via the Young's modulus  $E$ , Poisson's ratio  $\nu$  and the shell thickness  $h$ . The right-hand side of (2) represents the external virtual work and depends on the deterministic concentrated forces  $\mathbf{f}^{(j)}$  applied at the respective positions  $\mathbf{x}^{(j)}$  and the random distributed loading  $\mathbf{r}(\mathbf{x})$ . As will be detailed later, it is assumed that the loading applied by the train axles is composed of only vertical components so that both  $\mathbf{f}^{(j)}$  and  $\mathbf{r}(\mathbf{x})$  have only a non-zero vertical component. The random distributed train loading  $\mathbf{r}(\mathbf{x})$  is assumed to be a Gaussian process with a zero mean and known covariance, i.e.

$$\mathbf{r}(\mathbf{x}) = \begin{pmatrix} 0 \\ 0 \\ \mathcal{GP}(\mathbf{0}, c_r(\mathbf{x}, \mathbf{x}')) \end{pmatrix}. \quad (3)$$

Without loss of generality, the squared-exponential kernel is taken as a kernel

$$c_r(\mathbf{x}, \mathbf{x}') = \sigma_r^2 \exp\left(-\frac{\|\mathbf{x} - \mathbf{x}'\|^2}{2\ell_r^2}\right), \quad (4)$$

where  $\sigma_r$  is a scaling factor and  $\ell_r$  is a lengthscale parameter. Although the Euclidean squared-distance  $\|\mathbf{x} - \mathbf{x}'\|^2$  has been used, in structural mechanics it may be more appropriate to use the squared geodesic distance (Scarth et al., 2019).

The position and displacement vectors  $\mathbf{x}$  and  $\mathbf{u}(\mathbf{x})$  are discretised in the weak form (2) using basis functions obtained from Catmull-Clark subdivision surfaces (Cirak et al., 2000; Zhang et al., 2018). The weak form (2) depends on the curvature so that the FE basis functions must be smooth, or in other words, must have square-integrable second derivatives. Subdivision surfaces are the generalisation of

B-splines from computer-aided geometric design (CAGD) to unstructured meshes and provide smooth basis functions for discretising the position and displacement vectors  $\mathbf{x}$  and  $\mathbf{u}(\mathbf{x})$ . The resulting FE approach is referred to as isogeometric analysis (Hughes et al., 2005) and allows one to use the same representation for geometric design and analysis. Without going into further details, the subdivision basis functions  $\phi_i(\theta^1, \theta^2)$  furnish the two approximants

$$\mathbf{x}(\theta^1, \theta^2) = \sum_i \phi_i(\theta^1, \theta^2) \mathbf{x}_i, \quad \mathbf{u}(\theta^1, \theta^2) = \sum_i \phi_i(\theta^1, \theta^2) \mathbf{u}_i, \quad (5)$$

where  $\mathbf{x}_i$  is the coordinate and  $\mathbf{u}_i$  is the displacement of the FE node with the index  $i$  and  $(\theta^1, \theta^2)$  are parametric coordinates. The summations in (5) are over all the nodes in the FE mesh. After introducing (5) into the weak form (2) and numerically evaluating the integrals the linear system of equations

$$\mathbf{A}\mathbf{u} = \mathbf{f} \quad (6)$$

is obtained. Herein,  $\mathbf{A}$  is the stiffness matrix,  $\mathbf{u}$  is the nodal displacement vector and the force vector  $\mathbf{f}$  has the multivariate Gaussian density

$$\mathbf{f} \sim p(\mathbf{f}) = \mathcal{N}(\bar{\mathbf{f}}, \mathbf{C}_f), \quad (7)$$

where  $\bar{\mathbf{f}}$  is the mean vector and  $\mathbf{C}_f$  is the covariance matrix. Because the stiffness matrix  $\mathbf{A}$  is deterministic it is easy to show that the resulting random displacement vector has the probability density

$$\mathbf{u} \sim p(\mathbf{u}) = \mathcal{N}(\mathbf{A}^{-1}\bar{\mathbf{f}}, \mathbf{A}^{-1}\mathbf{C}_f\mathbf{A}^{-T}) = \mathcal{N}(\bar{\mathbf{u}}, \mathbf{C}_u). \quad (8)$$

Although not considered in this study, it is possible to consider uncertainties in the internal work in (2), such as random material parameters or geometry, leading to a random stiffness matrix  $\mathbf{A}$ , see Girolami et al. (2021) for details.

### 3.1.2. Bayesian inference

In the posited statistical model, the observed strain  $\mathbf{y}$  at the  $n_y$  sensor locations is assumed to be ultimately composed of three random components

$$\mathbf{y} = \mathbf{z} + \mathbf{e} = \rho\mathbf{P}\mathbf{u} + \mathbf{d} + \mathbf{e} = \mathbf{z} + \mathbf{e}. \quad (9)$$

That is, the observed strain  $\mathbf{y}$  is equal to the sum of the unknown (i.e. unobserved) ‘true’ strain  $\mathbf{z}$  and the Gaussian measurement error

$$\mathbf{e} \sim p(\mathbf{e}) = \mathcal{N}(\mathbf{0}, \mathbf{C}_e) \quad (10)$$

with a diagonal covariance matrix  $\mathbf{C}_e = \sigma_e^2\mathbf{I}$  and a standard deviation  $\sigma_e$ . In turn, the true system response  $\mathbf{z}$  is the linear combination of the FE strain  $\mathbf{P}\mathbf{u}$ , depending on the nodal displacements  $\mathbf{u}$ , and the mismatch, or model inadequacy, error  $\mathbf{d}$ . In the FE component,  $\rho$  is an unknown scaling parameter and  $\mathbf{P}$  is a matrix for obtaining the strain at sensor locations from the nodal displacement vector  $\mathbf{u}$ .

The random parameter  $\rho$  and the random mismatch error vector  $\mathbf{d}$  are the unknowns of the statistical model (9) and will be characterised using the measured strain data  $\mathbf{y}$  and the random FE solution  $\mathbf{u}$  in (8). The probability density of the mismatch error vector is assumed to be a multivariate Gaussian

$$\mathbf{d} \sim p(\mathbf{d}) = \mathcal{N}(\mathbf{0}, \mathbf{C}_d), \quad (11)$$

and the covariance matrix  $\mathbf{C}_d$  is obtained from the squared-exponential kernel

$$c_d(\mathbf{x}, \mathbf{x}') = \sigma_d^2 \exp\left(-\frac{\|\mathbf{x} - \mathbf{x}'\|^2}{2\ell_d^2}\right) \quad (12)$$

with the hyperparameters  $\sigma_d$  and  $\ell_d$ . In the following, the three hyperparameters of the statistical model are collected in the vector

$$\mathbf{w} := (\rho \ell_d \sigma_d)^\top. \quad (13)$$

We can now proceed in making statistical inference in light of the observed data  $\mathbf{y}$  and the posited statistical model (9). Since all the variables in the statistical model are Gaussians we can write by inspection, see e.g. [Murphy \(2012\)](#), for the likelihood

$$p(\mathbf{y}|\mathbf{u}, \mathbf{w}) = \mathcal{N}(\rho\mathbf{P}\mathbf{u}, \mathbf{C}_d + \mathbf{C}_e). \quad (14)$$

According to the Bayes rule, the posterior density of the FE solution and the hyperparameter vector is given by

$$p(\mathbf{u}, \mathbf{w}|\mathbf{y}) = \frac{p(\mathbf{y}|\mathbf{u}, \mathbf{w})p(\mathbf{u})p(\mathbf{w})}{p(\mathbf{y})} \quad (15a)$$

or

$$p(\mathbf{u}, \mathbf{w}|\mathbf{y}) \propto p(\mathbf{y}|\mathbf{u}, \mathbf{w})p(\mathbf{u})p(\mathbf{w}), \quad (15b)$$

where we have used the independence of the joint prior, i.e.  $p(\mathbf{u}, \mathbf{w}) = p(\mathbf{u})p(\mathbf{w})$ .

In statFEM we are interested in the conditioned posterior FE density

$$p(\mathbf{u}|\mathbf{y}) = \int p(\mathbf{u}, \mathbf{w}|\mathbf{y})p(\mathbf{w}|\mathbf{y}) d\mathbf{w}. \quad (16)$$

Following an empirical Bayes, or evidence approximation, approach, see e.g. [MacKay \(1999\)](#), this integral can be approximated by

$$p(\mathbf{u}|\mathbf{y}) \approx p(\mathbf{u}, \mathbf{w}^*|\mathbf{y}). \quad (17)$$

As a point estimate  $\mathbf{w}^*$  either the maximum

$$\mathbf{w}^* = \arg \max_{\mathbf{w}} p(\mathbf{w}|\mathbf{y}) \quad (18a)$$

or the mean

$$\mathbf{w}^* = \mathbb{E}[p(\mathbf{w}|\mathbf{y})] \quad (18b)$$

are suitable. When the hyperparameters are endowed with a prior  $p(\mathbf{w})$  the posterior  $p(\mathbf{w}|\mathbf{y}) \propto p(\mathbf{y}|\mathbf{w})p(\mathbf{w})$  can be considered for obtaining the point estimate. In this paper we sample  $p(\mathbf{w}|\mathbf{y})$  with the Markov-chain Monte Carlo method and take the empirical mean of the samples as  $\mathbf{w}^*$ . According to our statistical model (9), the (marginal) likelihood  $p(\mathbf{y}|\mathbf{w})$  is, by inspection, given by

$$p(\mathbf{y}|\mathbf{w}) = \mathcal{N}(\rho\mathbf{P}\bar{\mathbf{u}}, \mathbf{C}_d + \mathbf{C}_e + \rho^2\mathbf{P}\mathbf{C}_u\mathbf{P}^\top). \quad (19)$$



Finally, introducing the obtained point estimate  $\mathbf{w}^*$  in (15b) yields the sought posterior density  $p(\mathbf{u}|\mathbf{y})$ . To this end, note that the densities on the right-hand side of (15b) are Gaussians so that the posterior is a Gaussian as well. As shown in [Girolami et al. \(2021\)](#), the posterior density is given by

$$p(\mathbf{u}|\mathbf{y}) = \mathcal{N}(\bar{\mathbf{u}}_{|\mathbf{y}}, \mathbf{C}_{\mathbf{u}|\mathbf{y}}) \quad (20a)$$

with the covariance matrix

$$\mathbf{C}_{\mathbf{u}|\mathbf{y}} = \mathbf{C}_{\mathbf{u}} - \mathbf{C}_{\mathbf{u}}\mathbf{P}^T \left( \frac{1}{\rho^2} (\mathbf{C}_{\mathbf{d}} + \mathbf{C}_{\mathbf{e}}) + \mathbf{P}\mathbf{C}_{\mathbf{u}}\mathbf{P}^T \right)^{-1} \mathbf{P}\mathbf{C}_{\mathbf{u}} \quad (20b)$$

and the mean

$$\bar{\mathbf{u}}_{|\mathbf{y}} = \mathbf{C}_{\mathbf{u}|\mathbf{y}} \left( \rho\mathbf{P}^T (\mathbf{C}_{\mathbf{d}} + \mathbf{C}_{\mathbf{e}})^{-1} \mathbf{y} + \mathbf{C}_{\mathbf{u}}^{-1}\bar{\mathbf{u}} \right). \quad (20c)$$

With the determined posterior FE density we obtain for the the posterior true strain density

$$p(\mathbf{z}|\mathbf{y}) = \mathcal{N}(\rho\mathbf{P}\bar{\mathbf{u}}_{|\mathbf{y}}, \rho^2\mathbf{P}\mathbf{C}_{\mathbf{u}|\mathbf{y}}\mathbf{P}^T + \mathbf{C}_{\mathbf{d}}). \quad (21)$$

We considered so far only one single observation vector  $\mathbf{y}$  recorded at a fixed time instant  $t_k$ . The passage of a single train, however, leads to several hundreds of such observation vectors. We collect these vectors in a observation matrix

$$\mathbf{Y} = (\mathbf{y}_0 \ \mathbf{y}_1 \ \dots \ \mathbf{y}_{n_o}). \quad (22)$$

In principle, it is possible to consider each time instant  $t_k$  separately and to obtain for each a specific point estimate  $\mathbf{w}^*$  from (18). This can be very costly given that each computation requires the solution of an optimization problem or the sampling of a density with MCMC. More critically, the information content available in one single observation vector  $\mathbf{y}$  gives often only a very poor estimate for  $\mathbf{w}^*$ . As an aside, in case of MCMC a poor estimate is characterised by a very large empirical standard deviation for  $\mathbf{w}$ . Consequently, it is advantageous to consider all observation vectors simultaneously and to obtain one single  $\mathbf{w}^*$ . To this end, we first replace the mismatch error covariance kernel (12) with a scaled squared-exponential kernel

$$c_d(\mathbf{x}, \mathbf{x}', k) = (\gamma_k \sigma_d)^2 \exp \left( -\frac{\|\mathbf{x} - \mathbf{x}'\|^2}{2\ell_d^2} \right) \quad (23a)$$

with

$$\gamma_k = \frac{\|\mathbf{f}_k\|}{\max_k \|\mathbf{f}_k\|}, \quad (23b)$$

where each index  $k$  corresponds to a time instant  $t_k$  and  $\|\cdot\|$  denotes  $L_2$  norm. The scale factor  $\gamma_k$  is necessary because the number of axles on the bridge, hence load  $\mathbf{f}_k$  applied to the bridge at each time instant is different. As implied by our statistical model (9), it is necessary to scale each random vector  $\mathbf{d}_k$  in dependence of the magnitude of the observed strain  $\mathbf{y}_k$ , which is approximately proportional to the actual loading  $\mathbf{f}_k$ . Assuming statistical independence between the observations, the marginal likelihood

	main I-beams		transverse I-beams	
	web	flange	web	flange
thickness	25	120	16.5	27
height/width	2040	700	400	400

**Table 1.** Dimensions of the main and transverse I-beams (all in mm).

for determining  $\mathbf{w}^*$  is given by

$$p(\mathbf{Y}|\mathbf{w}) = \prod_{k=1}^{n_o} p(\mathbf{y}_k|\mathbf{w}) \quad (24a)$$

with

$$p(\mathbf{y}_k|\mathbf{w}) = \mathcal{N}(\rho\mathbf{P}\bar{\mathbf{u}}_k, \mathbf{C}_{d_k} + \mathbf{C}_e + \rho^2\mathbf{P}\mathbf{C}_{u_k}\mathbf{P}^\top). \quad (24b)$$

For further details, in particular with regards to implementation, we refer to [Girolami et al. \(2021\)](#).

### 3.2. FE model of the bridge superstructure

As discussed, the bridge superstructure is comprised of two identical main I-beams (east and west), 21 transverse I-beams, and a reinforced concrete deck. Given the double row of shear connectors present along the top of the transverse I-beam flanges, it is assumed that perfect shear transfer exists (i.e. composite action) between the transverse beams and the reinforced concrete deck. Therefore, all components are modelled using shell finite elements and are along joints rigidly connected to each other. The joints are able to transfer both forces and moments. In the FE model, the two main I-beams are 26.84 m long in accordance with Figure 2. Their top and bottom flanges are 0.7 m wide and their webs are 2.04 m deep and situated 7.3 m apart. The flanges consist, rather than doubler plates as shown in Figure 2, of a single plate with equivalent second moment of area. The 21 transverse I-beams are categorised into two groups: orthogonal and fanned. The orthogonal beams are located in the centre region of the superstructure and are placed at every 1.5 m; and, the fanned beams are situated near the two ends of the bridge. The flanges of the transverse beams are 0.4 m wide, and their webs are 0.4 m deep. The thickness of each component of the I-beams is given in Table 1.

The Young's modulus and Poisson's ratio of the steel I-beams are assumed to be  $E_s = 210$  GPa and  $\nu_s = 0.3$  respectively. The deck of the bridge is modelled without the ancillary structures such as the ballast and concrete sleepers. The thickness of the deck in the FE model is 0.25 m. An equivalent reinforced concrete elasticity modulus is used according to the rule of mixtures

$$E_{rc} = qE_s + (1 - q)E_c. \quad (25)$$

A steel reinforcement ratio of  $q = 0.03$  and a concrete elasticity modulus of  $E_c = 35$  GPa are assumed so that  $E_{rc} = 40.5$  GPa. The Poisson's ratio of the reinforced concrete is  $\nu_{rc} = 0.2$ .

Two different meshes as discretisations for the bridge superstructure are considered. Mesh M1 is a relatively coarse mesh consisting of 4635 nodes and 4600 quadrilateral elements and the finer mesh M2 consists of 7191 nodes and 7144 quadrilateral elements, see Figures 1 and 4. To model the rocker type supports of the bridge, pinned and roller supports at the FE nodes are applied.

Although there are data for the two different types of trains crossing the bridge, this paper focuses specifically on type T1 train (London Midland Class 350 Desiro) with four carriages and a total length of 81.47 m. According to [Lin et al. \(2019\)](#), the average normal axle load is 104 kN (52 kN per wheel). The speed of the train is assumed to be 131 km/h, hence the train crosses the bridge in less than three

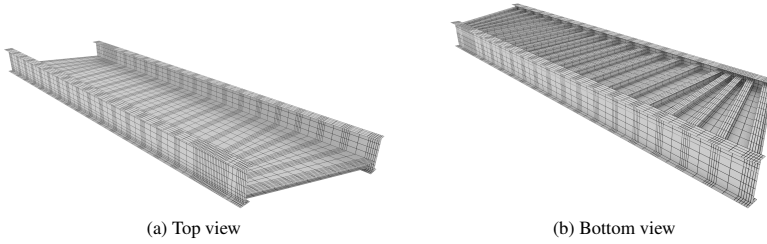


**Figure 4.** The fine FE mesh M2.

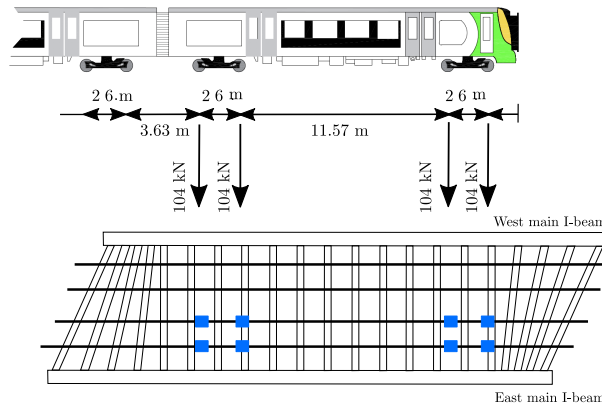


**Figure 5.** Applying loading as point loads centred at the train wheels. The point loads are directly applied to the deck rather than through ballasts. The axle weight of 104 kN is split into two point loads representing the two attached wheels.

seconds. The moving loads generated by the train wheels are directly applied to the concrete slab so that any load distribution by the track ballast is neglected. The moving point loads are centred at the axis of the wheels, as illustrated in Figure 5. Due to the relatively short span of the bridge, inertia effects are not taken into account. For a given set of wheel forces, depending on the position of the train, a single static analysis is performed.

The weight of the passing train is a random variable depending on a number of factors. To model this variation, a distributed random loading  $r(\mathbf{x})$ , which is a Gaussian process (3) with a covariance scaling parameter  $\sigma_r = 1000$  Pa and a length scale  $\ell_r = 1$  m, are applied. This is in addition to the wheel forces  $f^{(j)}$  of 52 kN per wheel (2).

#### 4. Results and discussion

Throughout this section, a train of type T1 with four carriages heading from north to south on the east track is considered. Specifically, the analysis and discussion involve the FBG measured axial strains along the top and bottom flanges of the east main I-beam. In statFEM, the axial strains are obtained by multiplying the nodal displacement vector  $\mathbf{u}$  with the projection matrix  $\mathbf{P}$ , which discretises the gradient operator and consists of the derivatives of the FE basis functions. Figure 6a depicts the total train load applied to the bridge over time depending on the number of train wheels on the bridge at a given time. The deflected superstructure at three distinct time instances is shown in Figure 6. It is evident that the

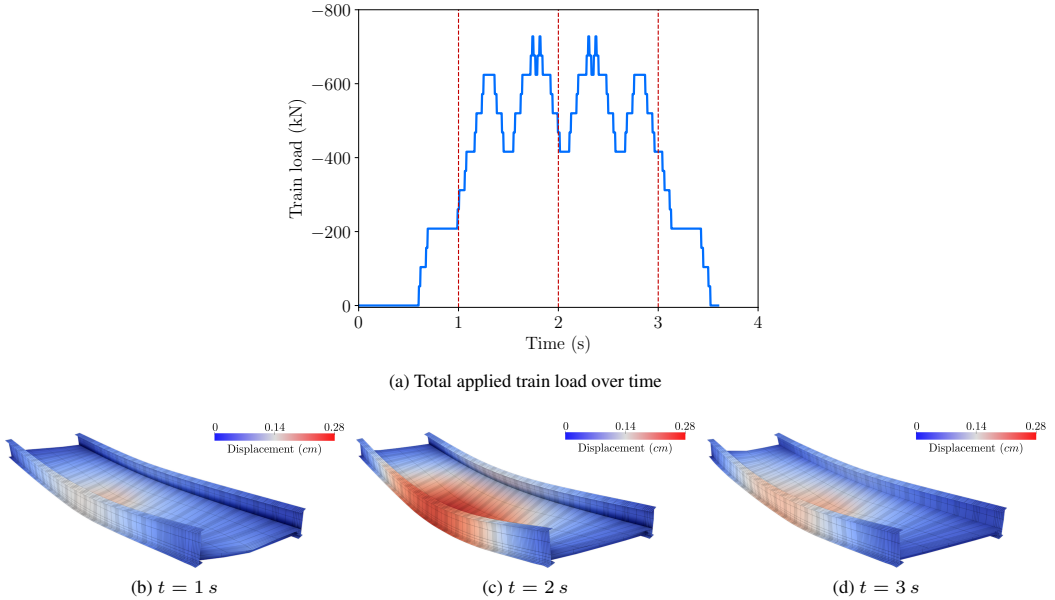


**Figure 6.** The train loading and the deflected bridge superstructure at three distinct time instances.

maximum displacement is always close to the midspan and its magnitude depends on the number of wheels present on the bridge at the given point in time.

#### 4.1. Mesh convergence and probabilistic FE analysis

The axial FE strains at the midspan of the east I-beam obtained using meshes M1 and M2 are plotted in Figure 7a. The results for both meshes are in close agreement and therefore, the coarser mesh M1 is deemed to be sufficient for the subsequent studies. The large-scale oscillations in the strains result from the changing number of train wheels on the bridge. The small-scale oscillations in the lower flange are due to the relative position of the wheel with respect to the relatively stiff transverse I-beams and the less stiff reinforced concrete deck.

The measured and computed FE strains at the midspan of the main I-beams are compared in Figure 7b. Each measured strain is depicted with a ‘+’. The small offset between the measured and FE strains in time indicates a mismatch between the actual and the assumed train speed. Although the FE strains are slightly smaller than the measured strains, their overall oscillation patterns are in close agreement. In comparison to the measured strains, the bottom flange FE strains have multiple small dips which is again related to the modelling of the connection between the main and transverse I-beams and the concrete deck. This is most likely due to the inability of the shell model to correctly represent the three-dimensional stress state at these connections.

The uncertainty in the train loading acting on the bridge yields according to (8) for the FE strains the prior probability density  $p(\mathbf{Pu})$ . The mean and the 95% confidence region of the strain profiles computed at 20 sensor locations along the top and bottom flanges of the east main I-beam (i.e. 40 sensor locations in total) are shown in Figure 9. The plotted curves are non-smooth because the strains are linearly interpolated between the sensor locations. The actual FE strains are smooth and are quadratic within each element (Zhang et al., 2018).

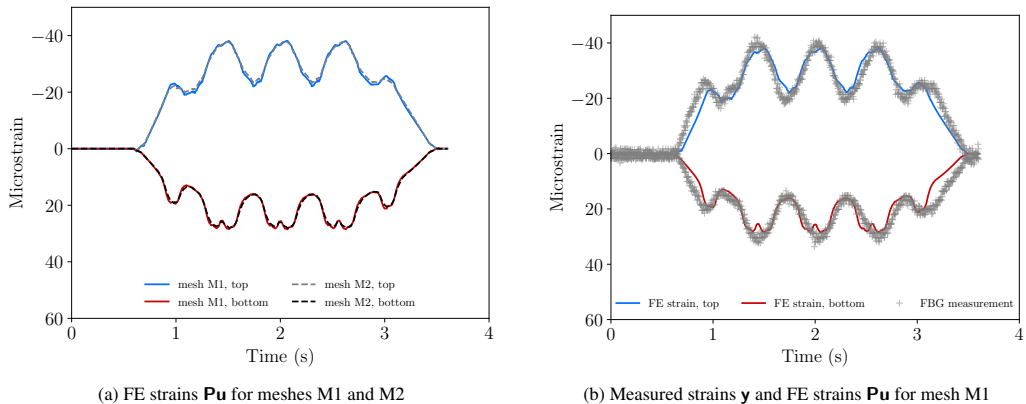


**Figure 7.** Axial strains along the top and bottom flanges of the east main I-beam at the midspan. .

	value
$\rho$	$0.8706 \pm 0.0037$
$\sigma_d$ (microstrain)	$4.0998 \pm 0.0263$
$\ell_d$ (meter)	$0.4261 \pm 0.0116$

**Table 2.** Empirical mean and standard deviation of  $p(\rho|\mathbf{Y})$ ,  $p(\sigma_d|\mathbf{Y})$ , and  $p(\ell_d|\mathbf{Y})$ .

## 4.2. Statistical finite element analysis

### 4.2.1. Inference of true strain response using all sensors

In this section, the recorded measurement data is used to predict the ‘true’ axial strains along the east main I-beam. The posterior FE strain density  $p(\mathbf{Pu}|\mathbf{y})$  and the true strain density  $p(\mathbf{z}|\mathbf{y})$  conditioned on the measured strains  $\mathbf{y}$  are given by (20) and (21). Evidently, the true strain response  $\mathbf{z}$  is unknown and only the measured strain response including some measurement error, i.e.  $\mathbf{y} = \mathbf{z} + \mathbf{e}$ , at the  $n_y$  locations is known. At each time instant  $t_k$ , the posterior FE strain density  $p(\mathbf{Pu}|\mathbf{y})$  and the true strain density  $p(\mathbf{z}|\mathbf{y})$  are computed from the measured strains  $\mathbf{y}_k$ . For simplicity, the subscript  $k$  is omitted here and in the following.

Before computing the posterior densities, the hyperparameter posterior  $p(\mathbf{w}|\mathbf{Y}) \propto p(\mathbf{Y}|\mathbf{w})p(\mathbf{w})$  with the marginal likelihood  $p(\mathbf{Y}|\mathbf{w})$  given in (24) must be determined. Recall, the components of the hyperparameter vector  $\mathbf{w}$  consist of the scaling parameter  $\rho$  and the covariance kernel parameters  $\sigma_d$  and  $\ell_d$  of the mismatch error  $\mathbf{d}$ . The strain recordings from all  $n_y = 40$  FBG sensors of the east main I-beam are considered in the observation (measurement) matrix  $\mathbf{Y} \in \mathbb{R}^{n_y \times n_o}$ . The position of the sensor measurement points are as indicated in Figure 3. Only data recorded during the passage of the train (i.e., within the time of passage  $1 \text{ s} \leq t \leq 3 \text{ s}$ , yielding  $n_o = 501$  sensor readings for each sensor) are considered. The standard deviation  $\sigma_e$  for the measurement error  $\mathbf{e}$  is estimated from the empirical standard deviation of the strain within  $0 \text{ s} \leq t \leq 0.5 \text{ s}$ , prior to the arrival of the train (see Figure 7b), which yields  $\sigma_e = 1$  microstrain. Due to insufficient prior knowledge of the true bridge response, we assume a non-informative prior density  $p(\mathbf{w}) \propto 1$  in sampling  $\mathbf{p}(\mathbf{w}|\mathbf{Y})$  using MCMC. In Figure 8 the normalised histograms for  $p(\rho|\mathbf{Y})$ ,  $p(\sigma_d|\mathbf{Y})$ , and  $p(\ell_d|\mathbf{Y})$  obtained with 20000 iterations and an acceptance ratio of 0.283 are shown. After determining the density of the hyperparameters  $p(\mathbf{w}|\mathbf{Y})$ , the posterior density of the FE strains  $p(\mathbf{Pu}|\mathbf{y})$  is calculated. As mentioned, the empirical mean  $\mathbf{w}^* = \mathbb{E}[\mathbf{w}]$  is used as a point estimate in calculating the posterior density  $p(\mathbf{Pu}|\mathbf{y})$  according to (20). The empirical mean and standard deviations of the three inferred hyperparameters are given in Table 2.

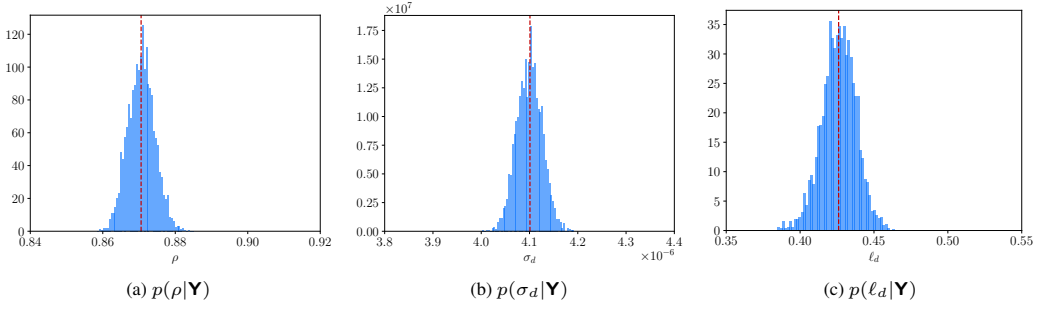


**Figure 8.** Posteriors of the hyperparameters  $\rho$ ,  $\sigma_d$  and  $\ell_d$  for  $n_y = 40$  and  $n_o = 501$  sampled with MCMC. The red dashed lines indicate the empirical means  $\rho^*$ ,  $\sigma_d^*$  and  $\ell_d^*$  of the samples.

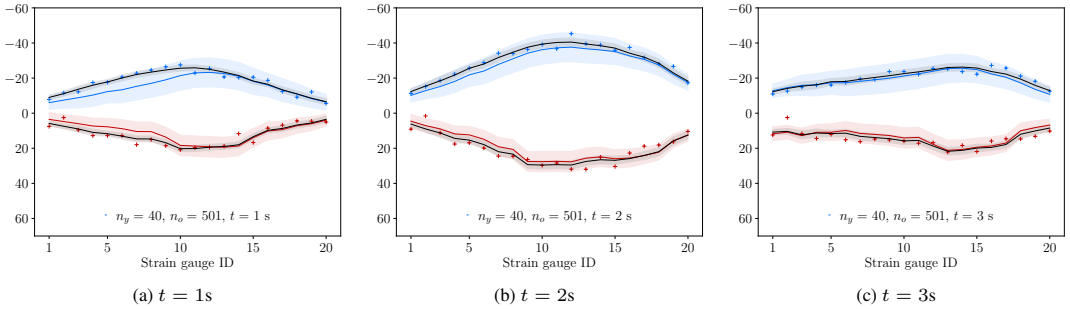


**Figure 9.** Posterior FE strain density  $p(\mathbf{P}\mathbf{u}|\mathbf{y})$  conditioned on strains (+) measured along the east main I-beam. The blue and red lines represent the mean  $\mathbf{P}\bar{\mathbf{u}}$  of the prior along the top and bottom flanges, respectively, and the black lines the conditioned mean  $\mathbf{P}\bar{\mathbf{u}}|\mathbf{y}$ . The shaded areas denote the corresponding 95% confidence regions. The unit of the vertical axis is microstrain.

Figure 9 depicts the prior and posterior densities of the axial FE strains and the measured strains at  $t = 1$  s,  $t = 2$  s, and  $t = 3$  s. For the FE strains, in addition to the mean, the corresponding 95% confidence regions are also plotted. Observe how the mean of the posterior FE strain lies much closer than the prior FE strain to the measured strains. It is also evident that the uncertainty in the prior FE strains is significantly reduced by conditioning them on the sensor measurements. In the corresponding Figure 10 the posterior densities of the true system response at  $t = 1$  s,  $t = 2$  s, and  $t = 3$  s are shown. The respective confidence regions encompass all the strain measurements and their mean is always visually very close to the mean of the data. These results clearly demonstrate that the FE strains conditioned on the measured strains (i.e. black lines in Figure 9), provide an improvement of strain prediction over the unconditioned FE strain results. Moreover, the 95% confidence regions provide a quantifiable method for identifying anomalous sensor readings.

#### 4.2.2. Inference of true strain response using a reduced number of sensors

Given the considerable efforts and costs associated with instrumenting operational structures, methods for optimizing both number and location of sensing points are critical. The statFEM approach allows for both data and physics-informed prediction even in situations where limited measurement data are available. In the following, a reduced number of measurements are considered to obtain the posterior of the FE strains  $p(\mathbf{P}\mathbf{u}|\mathbf{y})$  and the true strains  $p(\mathbf{z}|\mathbf{y})$ . A reduced number of sensors  $n_y$  and readings

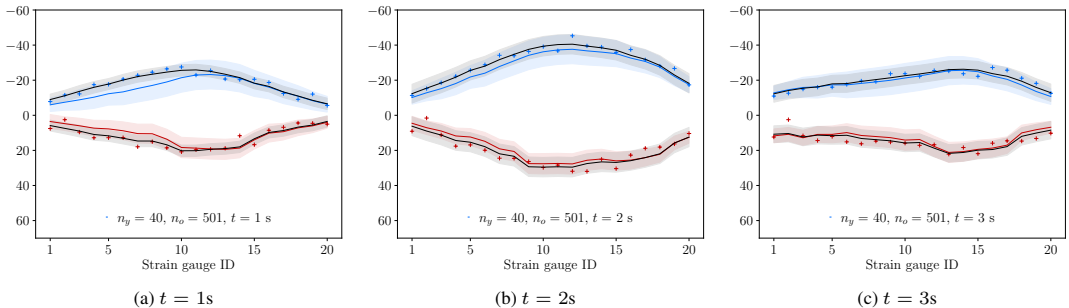


**Figure 10.** Inferred true strain density  $p(\mathbf{z}|\mathbf{y})$  conditioned on strains (+) measured along the east main I-beam. The blue and red lines represent the mean  $\mathbf{P}\bar{\mathbf{u}}$  of the prior along the top and bottom flanges, respectively, and the black lines the conditioned mean  $\bar{\mathbf{z}}_{\mathbf{y}}$ . The shaded areas denote the corresponding 95% confidence regions. The unit of the vertical axis is microstrain.

	gauge ID	top/bottom flange
$n_y = 40$	1, 2, 3, ..., 20	top & bottom
$n_y = 20$	1, 3, 5, ..., 19	top & bottom
$n_y = 10$	3, 7, 11, 15, 19	top & bottom

**Table 3.** Strain gauge ID for computations with  $n_y = \{40, 20, 10\}$  sensors located on the east main I-beam.

per sensor  $n_o$  are considered. The purpose of this study is to confirm the convergence of the two posteriors with increasing number of data and to determine the minimum number of required data for an acceptable estimate. The use of less data has advantages in terms of reduced instrumentation, increased numerical efficiency and the corresponding reduction in effort spent on data analysis and interpretation.

Three different number of sensing points  $n_y \in \{40, 20, 10\}$  along the east main I-beam are considered. In each case half of the sensing points are along the top and the other half along the bottom flange. Recall that the total number of sensors installed along the top and bottom flanges of each main I-beam are 40 (20 top and 20 bottom). Therefore, a subset of these sensing points is selected, with FBG sensor IDs for each  $n_y$  tabulated in Table 3. Furthermore, the number of strain measurements  $n_o$  is altered by selecting four different time intervals  $\Delta t = \{1/250 \text{ s}, 1/50 \text{ s}, 1/25 \text{ s}, 1 \text{ s}\}$  between the measurements within the observation window  $1 \text{ s} \leq t \leq 3 \text{ s}$ . The respective number of measurements are  $n_o = \{501, 101, 51, 3\}$ . As in the preceding section, the hyperparameter posterior  $p(\mathbf{w}|\mathbf{Y})$  is first determined. Then, the posterior  $p(\mathbf{w}|\mathbf{Y}) \propto p(\mathbf{Y}|\mathbf{w})p(\mathbf{w})$  is sampled with a non-informative prior  $p(\mathbf{w}) \propto 1$  using MCMC. For each combination of  $n_y$  and  $n_o$ , a total of 20000 MCMC samples are generated with an average acceptance ratio of 0.326.

The normalised histograms for  $p(\rho|\mathbf{Y})$ ,  $p(\sigma_d|\mathbf{Y})$ , and  $p(\ell_d|\mathbf{Y})$  for  $n_y = 20$  are shown in Figure 11. It is apparent that the standard deviations become significantly smaller with increasing number of readings  $n_o$ . The empirical mean and standard deviation for all combinations of  $n_y$  and  $n_o$  are given in the Tables 4, 5, and 6. As for  $n_y = 20$ , for  $n_y = 40$  and  $n_y = 10$  the standard deviation of the samples becomes smaller with increasing number of readings. A further key observation is that the standard deviation also becomes smaller when data from more sensors are considered (larger  $n_y$ ). For the scaling parameter  $\rho$ , the difference between the empirical means obtained with  $n_o = 501$  and  $n_o = 3$  is around 5% and decreases as additional readings are incorporated. For the mismatch parameter  $\sigma_d$ , the difference can be as high as 25%, and then decreases to 2–8% depending on the number of sensors  $n_y$ . It is remarkable

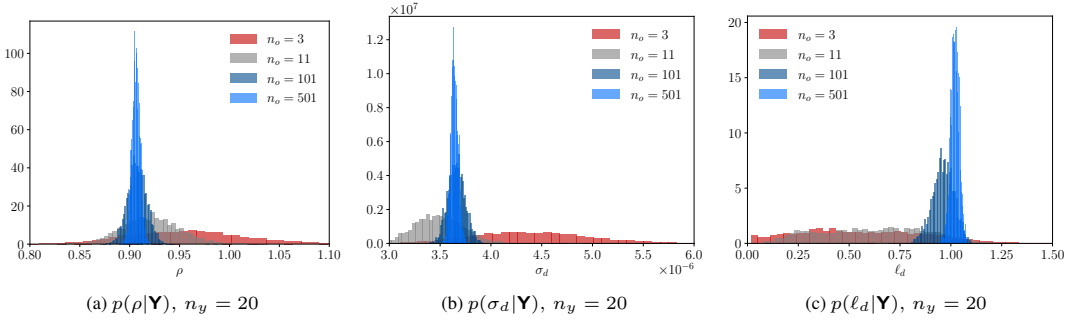


**Figure 11.** Posteriors of the hyperparameters  $\rho$ ,  $\sigma_d$  and  $\ell_d$  for  $n_y = 20$  and  $n_o \in \{3, 11, 101, 501\}$  sampled with MCMC.

	$n_y = 10$	$n_y = 20$	$n_y = 40$
$n_o = 3$	$1.0152 \pm 0.0717$	$0.9581 \pm 0.0593$	$0.9253 \pm 0.0548$
$n_o = 11$	$0.9614 \pm 0.0325$	$0.9215 \pm 0.0281$	$0.8869 \pm 0.0251$
$n_o = 101$	$0.9452 \pm 0.0103$	$0.9075 \pm 0.0093$	$0.8717 \pm 0.0080$
$n_o = 501$	$0.9457 \pm 0.0046$	$0.9062 \pm 0.0041$	$0.8706 \pm 0.0036$

**Table 4.** Empirical mean and standard deviation of  $p(\rho|\mathbf{Y})$ .

	$n_y = 10$	$n_y = 20$	$n_y = 40$
$n_o = 3$	$4.9211 \pm 1.0585$	$4.4129 \pm 0.6042$	$4.6830 \pm 0.4241$
$n_o = 11$	$3.5436 \pm 0.3651$	$3.4951 \pm 0.2365$	$3.9374 \pm 0.1742$
$n_o = 101$	$3.8462 \pm 0.1219$	$3.6611 \pm 0.0840$	$4.0894 \pm 0.0590$
$n_o = 501$	$3.8524 \pm 0.0542$	$3.6405 \pm 0.0367$	$4.0998 \pm 0.0263$

**Table 5.** Empirical mean and standard deviation of  $p(\sigma_d|\mathbf{Y})$ .

	$n_y = 10$	$n_y = 20$	$n_y = 40$
$n_o = 3$	$0.5657 \pm 0.4098$	$0.5634 \pm 0.3060$	$0.3766 \pm 0.1442$
$n_o = 11$	$0.4663 \pm 0.3378$	$0.6099 \pm 0.2592$	$0.2508 \pm 0.1250$
$n_o = 101$	$0.3736 \pm 0.1482$	$0.9628 \pm 0.5261$	$0.4335 \pm 0.0235$
$n_o = 501$	$0.4731 \pm 0.1005$	$1.0201 \pm 0.0208$	$0.4260 \pm 0.0116$

**Table 6.** Empirical mean and standard deviation of  $p(\ell_d|\mathbf{Y})$ .

that with 50 times less readings, the difference of the estimated  $\rho$  and  $\sigma_d$  is still acceptable. The length scale parameter  $\ell_d$ , however, shows a larger difference between the two smaller number of sensing points  $n_o = \{3, 11\}$  and the larger number of sensing points  $n_o = 501$ . This result, however, does not significantly affect the inferred posterior true strains.

Next, the posterior true strain density  $p(\mathbf{z}|\mathbf{y})$  is evaluated for different number of sensing points  $n_y$  and a fixed number of readings  $n_o = 11$ , see Figure 12. In contrast, Figure 13 shows the posterior true strains for different  $n_o$  and a fixed  $n_y = 10$ . It can be observed that the means  $\bar{\mathbf{z}}_{\mathbf{y}}$  obtained using less



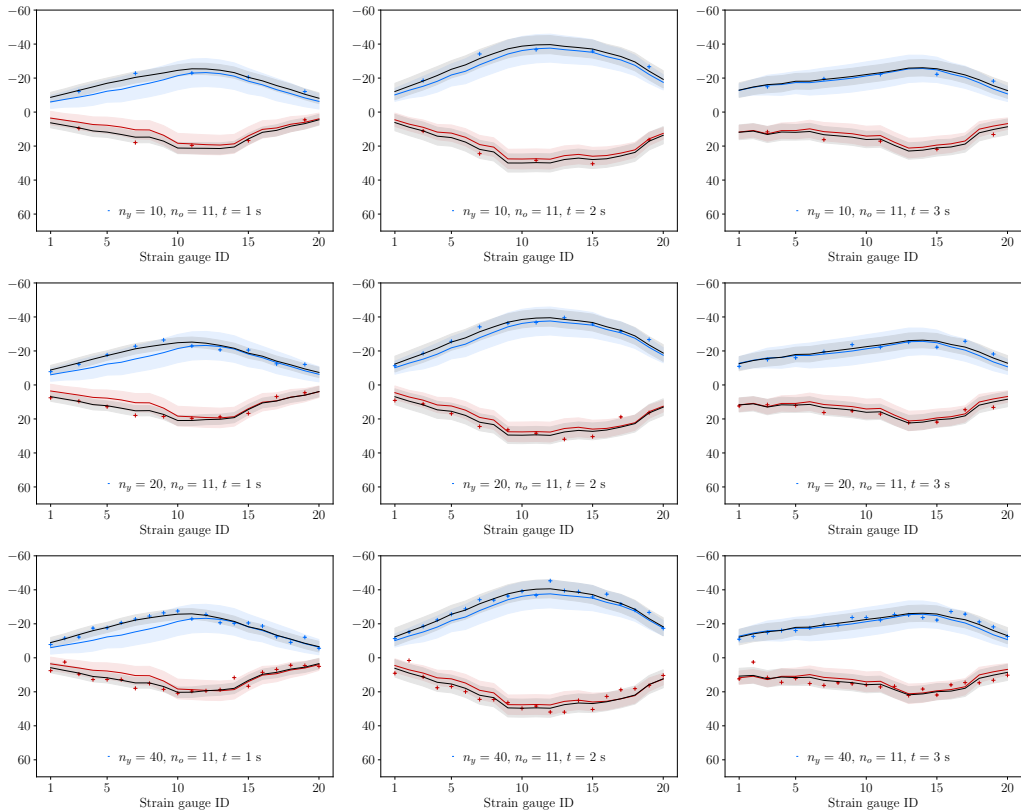


**Figure 12.** Inferred true strain density  $p(\mathbf{z}|\mathbf{y})$  conditioned on strains (+) measured along the east main I-beam. The blue and red lines represent the mean  $\mathbf{P}\bar{\mathbf{u}}$  of the prior along the top and bottom flanges, respectively, and the black lines the conditioned mean  $\bar{\mathbf{z}}_{|\mathbf{y}}$ . The shaded areas denote the corresponding 95% confidence regions. In each row the number of sensors  $n_y$  is constant. In each column the observation time  $t$  is constant. The unit of the vertical axis is microstrain.

observation data show close agreement with the ones obtained using more data. Similarly, the 95% confidence intervals of the different posteriors  $p(\mathbf{z}|\mathbf{y})$  look visually very similar for all combinations of  $n_o$  and  $n_y$ . These results confirm that it is possible to use data from fewer sensors  $n_y$  and fewer readings  $n_o$  to obtain a sufficiently reliable estimate for the true strain response.

#### 4.2.3. Predictive strains at non-sensor locations

Another advantage of the statFEM approach is its ability to generate strain predictions at locations at which no sensing data is available. Limited sensing points may arise due to cost and labour considerations but also, it is common in structural monitoring for sensor systems to malfunction and for entire sections of a sensor network to stop recording. The sensor strains along the west main I-beam are estimated by using only the readings from sensors installed along the east main I-beam. Although strain data along the west I-beam is available, they are not included in the observation matrix  $\mathbf{Y}$ . This test is an extreme case of missing measurement data due to either sensor malfunction or temporary system error.

Consider the vector of unobserved strains  $\hat{\mathbf{y}}$  at the locations with the coordinates  $\hat{\mathbf{X}}$ . The matrix  $\hat{\mathbf{X}}$  contains the coordinates of the FBG sensors along the west I-beam, see Figure 3. The predicted density

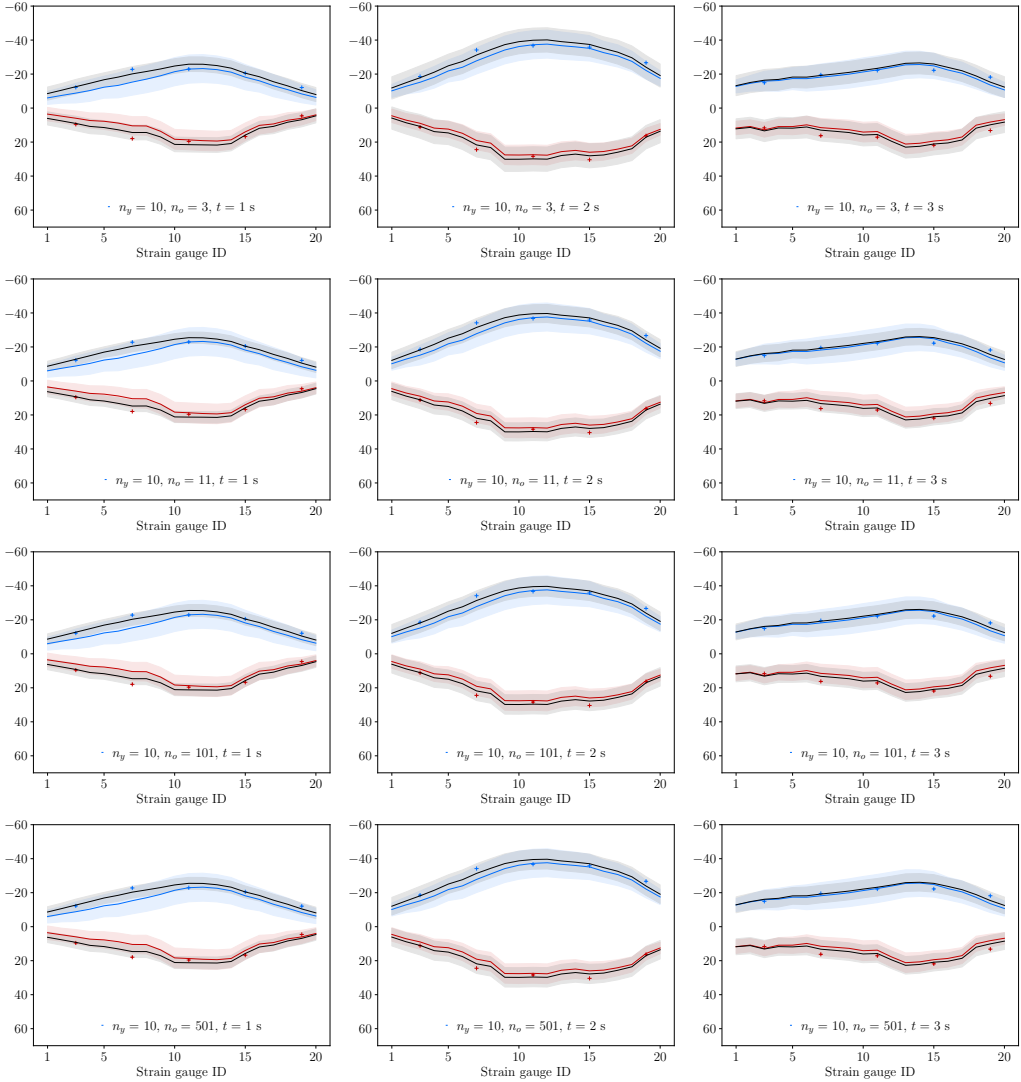


**Figure 13.** Inferred true strain density  $p(\mathbf{z}|\mathbf{y})$  conditioned on strains (+) measured along the east main I-beam. The blue and red lines represent the mean  $\mathbf{P}\bar{\mathbf{u}}$  of the prior along the top and bottom flanges, respectively, and the black lines the conditioned mean  $\bar{\mathbf{z}}_y$ . The shaded areas denote the corresponding 95% confidence regions. In each row the number of readings  $n_o$  is constant. In each column the observation time  $t$  is constant. The unit of the vertical axis is microstrain.

of sensors strains  $p(\hat{\mathbf{y}}|\mathbf{y})$  conditioned on the observations  $\mathbf{y}$  is given by

$$p(\hat{\mathbf{y}}|\mathbf{y}) = \int p(\hat{\mathbf{y}}|\mathbf{u})p(\mathbf{u}|\mathbf{y}) \, d\mathbf{u}. \quad (26)$$

With the likelihood (14) and the FE posterior (20) this becomes

$$p(\hat{\mathbf{y}}|\mathbf{y}) = \mathcal{N}\left(\rho\hat{\mathbf{P}}\bar{\mathbf{u}}_{|\mathbf{y}}, \rho^2\hat{\mathbf{P}}\mathbf{C}_{\mathbf{u}|\mathbf{y}}\hat{\mathbf{P}}^T + \hat{\mathbf{C}}_d + \hat{\mathbf{C}}_e\right), \quad (27)$$

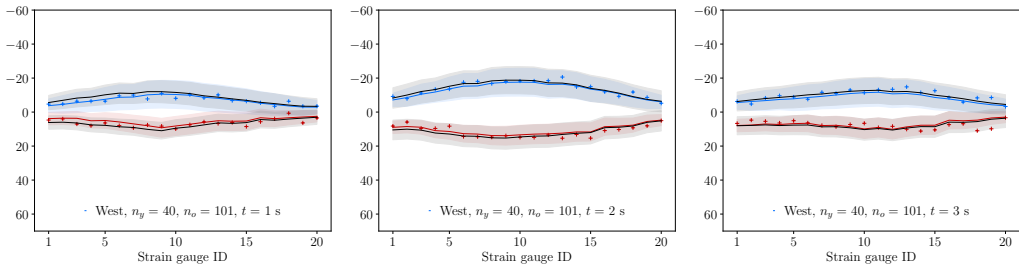


**Figure 14.** Predictive strain distribution  $p(\hat{\mathbf{y}}|\mathbf{y})$  along the west I-beam conditioned on strains (+) measured along the east main I-beam. The blue and red lines represent the mean  $\mathbf{P}\bar{\mathbf{u}}$  of the prior along the top and bottom flanges, respectively, and the black lines the predictive mean  $\rho\mathbf{P}\hat{\mathbf{u}}_{|\mathbf{y}}$ . The shaded areas denote the corresponding 95% confidence regions. The unit of the vertical axis is microstrain.

where the matrices  $\hat{\mathbf{P}}$ ,  $\hat{\mathbf{C}}_d$  and  $\hat{\mathbf{C}}_e$  are obtained by introducing the coordinates collected in  $\hat{\mathbf{X}}$  in the respective operator and covariance kernels. Note that this expression is very similar to the true system density  $p(\mathbf{z}|\mathbf{y})$  given in (21) up to the additional covariance term due to the measurement errors.

To evaluate the predictive strain density  $p(\hat{\mathbf{y}}|\mathbf{y})$ , the hyperparameters of the statistical model  $\mathbf{w}$  must first be learned as described previously. To this end, included in the observation matrix  $\mathbf{Y}$  are the strains of the  $n_y = 40$  sensors along the east I-beam and for each sensor the  $n_o = 101$  readings between the time  $1 \text{ s} \leq t \leq 3 \text{ s}$ . Subsequently,  $p(\hat{\mathbf{y}}|\mathbf{y})$  is obtained by introducing the point estimate  $\mathbf{w}^* = \mathbb{E}[\mathbf{w}]$  obtained by MCMC sampling into (27).

As shown in Figure 14, along the west I-beam, with only measurement data from the east I-beam taken into account, the predictive strain distribution  $p(\hat{\mathbf{y}}|\mathbf{y})$  is different from the prior FE computed strains  $p(\mathbf{P}\bar{\mathbf{u}})$  and the measured strains. Its mean  $\hat{\mathbf{y}}_{|\mathbf{y}}$  lies mostly in between the mean of the prior  $\mathbf{P}\bar{\mathbf{u}}$  and the measured strains. The 95% confidence regions of the predictive strain distribution and the prior have almost the same width. Hence, even at locations where there is no measurement data available, the statFEM analysis is able to improve the FE prior by utilising measurement data available from other parts of the bridge superstructure.

## 5. Conclusions

In this study, a statistical digital twin of a bridge superstructure has been developed which can combine continuous sensor measurements with FE model predictions to provide updated and real-time statistical predictions of strain distribution. The application of statFEM as a new modelling paradigm in creating digital twins was also introduced. By conditioning its predictions on measured strain data captured from 108 FBG sensors installed along the main superstructure of the operational railway bridge, the statFEM represents a new powerful probabilistic tool for assessing long-term structural monitoring data.

Based on the presented results, several conclusions can be drawn.

1. By considering strain data captured along the top and bottom flanges of the east and west main I-beams, the statFEM analysis showed an improvement of the mean strain estimates after being conditioned on the recorded sensor data. The 95% confidence bounds provided a quantifiable means for identifying anomalous sensor readings, which represents a significant step change in how structural monitoring data may be more reliably interpreted.
2. To evaluate the effect that the number of sensing points has on statFEM predictions, several sensor subsets (40, 20 and 10 sensors) for each main I-beam were considered in the analysis. The resulting predictive strain distributions and associated 95% confidence bounds between the three

sensor subsets were negligible. This demonstrated that the statFEM approach may be used to optimize sensor network design leading to significant reductions in instrumentation costs.

3. In addition to evaluating the effect of a reduced number of sensing points, several reduced sampling rates for each individual FBG sensor (originally capturing data at 250 Hz) were considered. Once again, the statFEM approach proved to provide robust mean estimates of the predictive strains regardless of sampling rate.
4. Using only strain data captured along the east main I-beam, the predictive strain distribution along the west main I-beam was estimated. It was shown that the predictive mean along the west I-beam incorporates the effects from both the FE prior and the measured data at the opposite east main I-beam. Therefore, in cases where missing or damaged parts of a sensor network exist, the statFEM approach can still be used to generate meaningful interpretations of the data.

This study has highlighted the suitability of statFEM, in combination with modern cloud-based data collection and storage infrastructure (Souza et al., 2018), for continuous, real-time monitoring and condition assessment of infrastructure assets. As evident from the results presented, a relatively coarse FE model is sufficient to obtain reliable predictions. Such FE models can be analysed in near-real time on a cloud-based computing environment enabling the viable creation of a digital twin. Furthermore, in determining the 'true' system response, the costly MCMC sampling of the hyperparameters used in this paper can be replaced with a more efficient optimisation algorithm, like L-BFGS-B (Zhu et al., 1997). The choice of a suitable coarse FE model can be rationalised with the powerful Bayesian model selection paradigm (Beck, 2010; Girolami et al., 2021). Indeed, this paradigm provides also a means to discover sudden changes in the state of the infrastructure by comparing the plausibility of different predefined response mechanisms.

## References

- Abdulkarem, M, Samsudin, K, Rokhani, F. Z, and Rasid, M. F. A (2020). Wireless sensor network for structural health monitoring: A contemporary review of technologies, challenges, and future direction. *Structural Health Monitoring*, 19:693–735.
- Arendt, P. D, Apley, D. W, and Chen, W (2012). Quantification of model uncertainty: Calibration, model discrepancy, and identifiability. *Journal of Mechanical Design*, 134:100908:1–100908:12.
- Bayarri, M. J, Berger, J. O, Paulo, R, Sacks, J, Cafeo, J. A, Cavendish, J, Lin, C.-H, and Tu, J (2007). A framework for validation of computer models. *Technometrics*, 49:138–154.
- Beck, J. L (2010). Bayesian system identification based on probability logic. *Structural Control and Health Monitoring*, 17:825–847.
- Bolton, A, Enzer, M, Schooling, J, et al. (2018). The gemini principles: Guiding values for the national digital twin and information management framework. Technical report, Centre for Digital Built Britain and Digital Framework Task Group.
- Brownjohn, J. M. W (2007). Structural health monitoring of civil infrastructure. *Philosophical Transactions of the Royal Society A: Mathematical, Physical and Engineering Sciences*, 365:589–622.
- Butler, L. J, Lin, W, Xu, J, Gibbons, N, Elshafie, M. Z. E. B, and Middleton, C. R (2018). Monitoring, modeling, and assessment of a self-sensing railway bridge during construction. *Journal of Bridge Engineering*, 23:1–16.
- Cirak, F and Long, Q (2011). Subdivision shells with exact boundary control and non-manifold geometry. *International Journal for Numerical Methods in Engineering*, 88:897–923.
- Cirak, F, Ortiz, M, and Schröder, P (2000). Subdivision surfaces: A new paradigm for thin-shell finite-element analysis. *International Journal for Numerical Methods in Engineering*, 47:2039–2072.
- Cirak, F, Scott, M. J, Antonsson, E. K, Ortiz, M, and Schröder, P (2002). Integrated modeling, finite-element analysis, and engineering design for thin-shell structures using subdivision. *Computer-Aided Design*, 34:137–148.
- De Battista, N, Cheal, N, Harvey, R, and Kechavarzi, C (2017). Monitoring the axial displacement of a high-rise building under construction using embedded distributed fibre optic sensors. In *SHMII 2017 - 8th International Conference on Structural Health Monitoring of Intelligent Infrastructure, Proceedings*, pages 1058–1067.
- Di, J, Ruan, X, Zhou, X, Wang, J, and Peng, X (2021). Fatigue assessment of orthotropic steel bridge decks based on strain monitoring data. *Engineering Structures*, 228:111437.
- Di Murro, V, Pelecanos, L, Soga, K, Kechavarzim, C, and Morton, R (2016). Distributed fibre optic long-term monitoring of concrete-lined tunnel section tt10 at cern. In *International Conference on Smart Infrastructure and Construction*.
- Frangopol, D. M and Soliman, M (2016). Life-cycle of structural systems: recent achievements and future directions. *Structure and Infrastructure Engineering*, 12:1–20.
- Ghanem, R. G and Spanos, P. D (1991). *Stochastic Finite Elements: A Spectral Approach*. Springer.

- Girolami, M, Febrianto, E, Yin, G, and Cirak, F** (2021). The statistical finite element method (statFEM) for coherent synthesis of observation data and model predictions. *Computer Methods in Applied Mechanics and Engineering*, 375:113533:1–113533:32.
- Huang, Y, Shao, C, Wu, B, Beck, J. L, and Li, H** (2019). State-of-the-art review on Bayesian inference in structural system identification and damage assessment. *Advances in Structural Engineering*, 22:1329–1351.
- Hughes, T. J. R, Cottrell, J. A, and Bazilevs, Y** (2005). Isogeometric analysis: CAD, finite elements, NURBS, exact geometry and mesh refinement. *Computer Methods in Applied Mechanics and Engineering*, 194:4135–4195.
- Kaipio, J and Somersalo, E** (2006). *Statistical and computational inverse problems*. Springer.
- Kennedy, M. C and O’Hagan, A** (2001). Bayesian calibration of computer models. *Journal of the Royal Statistical Society: Series B (Statistical Methodology)*, 63:425–464.
- Lau, F. D.-H, Adams, N. M, Girolami, M. A, Butler, L. J, and Elshafie, M. Z. E. B** (2018). The role of statistics in data-centric engineering. *Statistics & Probability Letters*, 136:58–62.
- Lin, W, Butler, L. J, Elshafie, M. Z. E. B, and Middleton, C. R** (2019). Performance assessment of a newly constructed skewed half-through railway bridge using integrated sensing. *Journal of Bridge Engineering*, 24:1–14.
- Lynch, J. P** (2007). An overview of wireless structural health monitoring for civil structures. *Philosophical Transactions of the Royal Society A: Mathematical, Physical and Engineering Sciences*, 365:345–372.
- MacKay, D. J. C** (1992). Bayesian interpolation. *Neural Computation*, 4:415–447.
- MacKay, D. J. C** (1999). Comparison of approximate methods for handling hyperparameters. *Neural Computation*, 11:1035–1068.
- Malekzadeh, M, Atia, G, and Catbas, F. N** (2015). Performance-based structural health monitoring through an innovative hybrid data interpretation framework. *Journal of Civil Structural Health Monitoring*, 5:287–305.
- Murphy, K. P** (2012). *Machine learning: a probabilistic perspective*. MIT press.
- Oden, J. T, Moser, R, and Ghattas, O** (2010). Computer predictions with quantified uncertainty, Part i. *SIAM News*, 43:1–3.
- Pasquier, R and Smith, I** (2016). Iterative structural identification framework for evaluation of existing structures. *Engineering Structures*, 106:179 – 194.
- Rasheed, A, San, O, and Kvamsdal, T** (2020). Digital twin: Values, challenges and enablers from a modeling perspective. *IEEE Access*, 8:21980–22012.
- Santner, T. J, Williams, B. J, and Notz, W. I** (2018). *The design and analysis of computer experiments*. Springer, 2nd edition edition.
- Scarth, C, Adhikari, S, Cabral, P. H, Silva, G. H. C, and do Prado, A. P** (2019). Random field simulation over curved surfaces: Applications to computational structural mechanics. *Computer Methods in Applied Mechanics and Engineering*, 345:283–301.
- Souza, V. B, Masip-Bruin, X, Marín-Tordera, E, Sánchez-López, S, Garcia, J, Ren, G.-J, Jukan, A, and Ferrer, A. J** (2018). Towards a proper service placement in combined Fog-to-Cloud (F2C) architectures. *Future Generation Computer Systems*, 87:1–15.
- Stuart, A. M** (2010). Inverse problems: a Bayesian perspective. *Acta Numerica*, 19:451–559.
- Sudret, B and Der Kiureghian, A** (2000). Stochastic finite element methods and reliability: a state-of-the-art report. Technical Report UCB/SEMM-2000/08, Department of Civil & Environmental Engineering, University of California, Berkeley.
- Tsiliamanis, G, Wagg, D. J, Dervilis, N, and Worden, K** (2021). On generative models as the basis for digital twins. *Data-Centric Engineering*, 2.
- Worden, K, Cross, E, Barthorpe, R, Wagg, D, and Gardner, P** (2020). On digital twins, mirrors, and virtualizations: Frameworks for model verification and validation. *ASCE-ASME J Risk and Uncert in Engrg Sys Part B Mech Engrg*, 6(3).
- Wu, R.-T and Jahanshahi, M. R** (2020). Data fusion approaches for structural health monitoring and system identification: Past, present, and future. *Structural Health Monitoring*, 19:552–586.
- Ye, C, Butler, L, Bartek, C, Iangurazov, M, Lu, Q, Gregory, A, Girolami, M, and Middleton, C** (2019). A digital twin of bridges for structural health monitoring. In *12th International Workshop on Structural Health Monitoring 2019*.
- Zhang, Q, Sabin, M, and Cirak, F** (2018). Subdivision surfaces with isogeometric analysis adapted refinement weights. *Computer-Aided Design*, 102:104–114.
- Zhu, C, Byrd, R. H, Lu, P, and Nocedal, J** (1997). Algorithm 778: L-BFGS-B: Fortran subroutines for large-scale bound-constrained optimization. *ACM Transactions on Mathematical Software (TOMS)*, 23:550–560.